

Composite Analysis-Based Machine Learning for Prediction of Tropical Cyclone-Induced Sea Surface Height Anomaly

Hongxing Cui^{ID}, Danling Tang^{ID}, Huizeng Liu^{ID}, Yi Sui, and Xiaowei Gu^{ID}

Abstract—Sea surface height anomaly (SSHA) induced by tropical cyclones (TCs) is closely associated with oscillations and is a crucial proxy for thermocline structure and ocean heat content in the upper ocean. The prediction of TC-induced SSHA, however, has been rarely investigated. This study presents a new composite analysis-based random forest (RF) approach to predict daily TC wind pump induced SSHA. The proposed method utilizes TC's characteristics and prestorm upper oceanic parameters as input features to predict TC-induced SSHA up to 30 days after TC passage. Simulation results suggest that the proposed method is skillful at inferring both the amplitude and temporal evolution of SSHA induced by TCs of different intensity groups. Using a TC-centered $5^\circ \times 5^\circ$ box, the proposed method achieves highly accurate prediction of TC-induced SSHA over the Western North Pacific with root mean square error of 0.024 m, outperforming alternative machine learning methods and the numerical model. Moreover, the proposed method also demonstrated good prediction performance in different geographical regions, i.e., the South China Sea and the Western North Pacific subtropical ocean. The study provides insight into the application of machine learning in improving the prediction of SSHA influenced by extreme weather conditions. Accurate prediction of TC-induced SSHA allows for better preparedness and response, reducing the impact of extreme events (e.g., storm surge) on people and property.

Index Terms—Composite analysis, machine learning, random forest, sea surface height anomaly, tropical cyclones.

Manuscript received 24 October 2022; revised 30 January 2023; accepted 17 February 2023. Date of publication 22 February 2023; date of current version 16 March 2023. This work was supported in part by the Key Special Supporting Talent Team Project of Guangdong under Grant 2019BT02H594, in part by Key Special Project of Southern Marine Science and Engineering Guangdong Laboratory (Guangzhou) (for Introduced Talents Team) under Grant GML2021GD0810, and in part by National Natural Science Foundation of China under Grant 41876136. (*Corresponding author: Danling Tang*.)

Hongxing Cui is with the Southern Marine Science and Engineering Guangdong Laboratory (Guangzhou), Guangdong Remote Sensing Center for Marine Ecology and Environment, Guangzhou 511458, China, and also with the Department of Ocean Science, Hong Kong University of Science and Technology, Hong Kong (e-mail: hcui@connect.ust.hk).

Danling Tang is with the Southern Marine Science and Engineering Guangdong Laboratory (Guangzhou), Guangdong Remote Sensing Center for Marine Ecology and Environment, Guangzhou 511458, China (e-mail: lingzistd@126.com).

Huizeng Liu is with the Institute for Advanced Study, Shenzhen University, Shenzhen 518060, China (e-mail: huizeng.liu@szu.edu.cn).

Yi Sui is with the Department of Oceanography, Dalhousie University, Halifax, NS B3H 4R2, Canada, and also with the Southern Marine Science and Engineering Guangdong Laboratory (Guangzhou), Guangdong Remote Sensing Center for Marine Ecology and Environment, Guangzhou 511458, China (e-mail: yisui@dal.ca).

Xiaowei Gu is with the School of Computing, University of Kent, Canterbury CT2 7NZ, U.K. (e-mail: x.gu@kent.ac.uk).

Digital Object Identifier 10.1109/JSTARS.2023.3247881

I. INTRODUCTION

TROPICAL cyclone (TC) has strongly positive wind stress curl over the sea surface, which is an intensive forcing [1], [2]. The passage of the TC generates oscillation in the upper ocean, including mainly both baroclinic and barotropic modes [3], [4]. The isopycnal displacements involved in the thermocline, and the triggering of near-inertial oscillations in one spreading three-dimensional pattern, are related to the baroclinic mode [2]. The barotropic mode has a cyclonically rotating current field and is connected to the geostrophic sea surface depression of 20–30 cm [5]. Gradients presented in the TC-induced sea surface height (SSH) produce a time-dependent barotropic response [3]. Moreover, TC wind pump generated SSH anomalies (SSHAs) have a considerable effect on the ocean's dynamic and thermodynamic structure, as well as on regulating ocean–atmosphere interaction at various spatial-temporal scales [6], [7]. The temporal evolution of the SSHA after the TC passage can be used to infer the changes in the thermocline and upper ocean heat content [8], which is a proxy to reveal propagations of planetary Kelvin and Ross waves [9], [10], [11]. Furthermore, TC-induced SSHA plays a vital role in explaining the mechanisms of marine ecology driven by TC wind pump [12], [13]. Despite of the importance, the accurate prediction of TC-induced SSHA remains a highly challenging task to be further explored.

A few studies on SSHA prediction and TC observations have been carried out in recent years. For SSHA predictions, methods can be generally classified into physical-based and data-driven approaches. Physical-based approaches combine related physical and dynamical equations to calculate sea-level changes. For example, an Earth system model with a dynamic three-dimensional ocean was developed by Srivastava et al. [14] to quantify the effect of observational constraints on thermosteric sea-level rise. A hydrological model was proposed by Chen et al. [15] to forecast the global mean sea level. A key issue associated with physical-based approaches lies in providing the initial conditions on the particular oceanic characteristics.

On the other hand, data-driven approaches use the sea surface height records to model the latent relationship between the SSHA and environmental variables. For example, in the Eastern Equatorial Pacific, a polynomial-harmonic model with the least-squares method was proposed to predict the gridded

SSHA [16]. Along the mid-Atlantic, based on the empirical model decomposition, in the North Atlantic, a multivariate autoregressive method was proposed to predict the seasonal SSHA variability [17]. Data-driven approaches can predict the SSHA very well with a lower demand of prior knowledge.

A number of novel TC observation approaches have also been proposed. For example, Horstman et al. [18] presented algorithms for retrieving high-resolution wind fields from synthetic aperture radar (SAR) data in TC conditions. Wang et al. [19] presented a brand-new scanning method, that uses three downward-pointing and conically scanning beams for a future spaceborne Doppler weather radar mission to capture 3-D wind fields of TCs. One spaceborne version of the velocity-azimuth display (VAD) method was proposed for wind field retrieval [20]. However, there is still a lack of effective approaches to predict SSHA after TC passage.

The change of SSHA is continuous in both time and space domains. Previous aforementioned studies have successfully predicted the smoothed SSHA, that is, this SSHA without considering specific extreme events, such as TCs. In other words, the amplitude of smoothed SSHA is very weak, while the intensive amplitude of SSHA is generated by the barotropic mode driven by TCs [3], [4]. Strong TC leads to a strong signal-to-noise ratio of SSHA after the TC passage [8], [21]. The signal-to-noise ratio associated with TC intensity varies significantly, resulting in an unbalanced distribution of TC-induced SSHA. Such unbalanced distribution in data makes it difficult in predicting the nonlinear relationship between SSHA and other environmental factors. Moreover, there is a lack of spatial and temporal continuity in data for TC occurrences from case to case, which makes predicting TC-induced SSHA more challenging. To the best of the authors' knowledge, this issue has rarely been investigated using ML methods in studies before. As the SSHA is an important parameter in the study of ocean dynamics and marine ecology under the influence of TCs [6], [7], [8], [9], [10], [11], [12], it is essential to develop a straightforward and robust method to predict the TC-induced SSHA. Above all, accurate prediction of TC-induced SSHA enables better response and preparation, reducing the impact of extreme events (e.g., storm surge) on people and property.

In order to accurately predict the daily TC-induced SSHA and its temporal evolution, this study proposes a composite analysis-based random forest (RF) method. The main reason for employing the RF method is that it has been successfully applied in fields related to the ocean and climate change [22], [23]. Composite analysis can effectively enhance the signal-to-noise ratio by averaging values in a TC-centered box, which makes it easier for the RF method to learn from oceanic and atmospheric parameters. The performance of the proposed method is systematically evaluated for temporal evolution and spatial distribution of the area-averaged composite SSHA. The sensitivity of TC-centered box size on the prediction accuracy of the proposed method is also investigated. Then the proposed method is evaluated in two distinct geographical regions, e.g., the South China Sea (SCS) and the Western North Pacific subtropical ocean (WNPSO). The study demonstrates the stable prediction performance of the proposed method over these two regions.

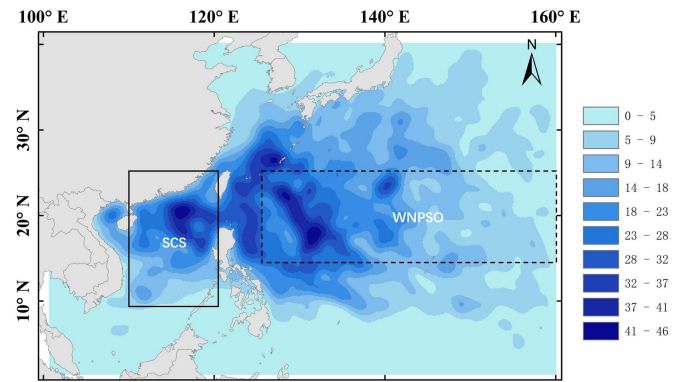


Fig. 1. Density of TC centers, with colors representing the number of TC centers at 6-h intervals from January 1998 to December 2018, and the spatial resolution is $0.1^\circ \times 0.1^\circ$. The solid rectangle encloses the SCS; the dashed rectangle encloses the WNPSO.

TABLE I
UPPER-OCEAN FACTORS AND THEIR UNITS, SENSORS, AND BANDS

Parameters	Unit	Sensors/Model	Band
SSH	m	Radar altimeter	Ku-Band
SST	°C	TMI, AMSR-E, AMSR2, WindSat, GMI	L-Band
U	m/s	Model	—
V	m/s	Model	—
MLD	m	Model	—
T100	°C	Model	—

Note: ‘—’ means data assimilation of satellite and in situ observations.

Finally, the differences between the numerical model products and ML-based predictions are also discussed.

II. DATA AND METHODS

A. Study Area

Tropical cyclones frequently occur in the Western North Pacific (WNP). On average, more than a third of worldwide TC occurs in the WNP, with some of the strongest TC occurring in specific years. The study area, WNP, is defined as the area between 0 and 40 °N, 100 and 160°E (see Fig. 1). To evaluate the performance of the proposed method in different geographical regions, we selected two regions where the most violent TCs occur, i.e., the SCS and the WNPSO [24], [25]. The SCS and the WNPSO are defined as the areas 10–25°N, 110–120°E, and 15–25°N, 125–160°E, respectively.

B. Data

The study period runs from 1998 to 2018. Three main datasets were used, and six upper-ocean parameters were extracted (Table I):

- 1) *Observational data:* Daily altimeter satellite gridded sea level anomalies, with a spatial resolution of $0.25^\circ \times 0.25^\circ$, are estimated by Optimal Interpolation and merging the measurements from multiple altimeter missions available (e.g., Jason-1, Jason-2, Jason-3, Sentinel-3A, and HY-2B). The SSH data can be retrieved from the EU Copernicus

TABLE II
INPUT FEATURES ABBREVIATION AND THEIR EXPLANATIONS

Abbreviation	Explanations
V_{max}	Maximum 1-min sustained surface wind speed of TC
V_{trans}	Translation speed of TC
$R30$	The shortest radius of 30kt winds or greater of TC
\overline{SSHA}	Average of sea surface height anomaly within prestorm five days
\overline{SSTA}	Average of sea surface temperature anomaly within prestorm five days
$\overline{T100A}$	Average of potential temperature anomaly at 100m within prestorm five days
\overline{MLDA}	Average of mixed layer depth anomaly within prestorm five days
\overline{UgResA}	Average of vertical shear of zonal current speed anomaly within prestorm five days
\overline{VgResA}	Average of vertical shear of meridional current speed anomaly within prestorm five days

Marine Environment Monitoring Service (CMEMS). The Optimally Interpolated daily SST products, using the microwave data (MW) [26], with a spatial resolution of $0.25^\circ \times 0.25^\circ$, are available from Remote Sensing Systems. Cloudy conditions have little effect on this study because the microwave has an advantage in penetrating clouds.

- 2) *Reanalysis data:* Daily global reanalysis multiensemble product GREP provides mixed layer depth (MLD), potential temperature, eastward current speed (U), and northward current speed (V). The reanalysis dataset has 75 levels in its vertical grid (from 0 to 5500 m). The spatial resolution of each layer is $0.25^\circ \times 0.25^\circ$. The reanalysis data used in this study can be available from the CMEMS, which is widely used in ocean studies [27].
- 3) *Best TC-track data:* The TC Best-track data were produced by the Japan Meteorological Agency (JMA) and obtained from the International Best Track Archive for Climate Stewardship (IBTrACS) archive [28]. The best-track data include TC's intensity, translation speed, the shortest radius of 30kt winds or greater, and TC-centered locations measured at a 6-h interval.

C. Data Preprocessing and Composite Analysis

The TC-induced SSHA is highly related to atmospheric and oceanic variables. A total of nine variables, associated with TC characteristics and prestorm upper-ocean conditions, were considered as input features (see Table II). The first three variables related to TC are intensity (V_{max}), translation speed of storms (V_{trans}), and radius ($R30$). The translation speed, i.e., V_{trans} , for each TC was then calculated as the distance between neighboring TC-centered positions divided by 6 h. To follow the Saffir–Simpson hurricane wind scale, the JMA data are converted from 10-min mean values to 1-min mean values by utilizing the Koba table [29]. The maximum 1-min sustained surface wind speed is represented by V_{max} .

The mean values of six predictors of the upper ocean from prestorm 0 to 4 days are the other six input variables, denoted by \overline{MLDA} , \overline{SSHA} , \overline{SSTA} , $\overline{T100A}$, \overline{UgResA} , and \overline{VgResA} . The variable with an overline indicates the average of each variable over the five days before the TC. Among them, the \overline{MLDA} is the

MLD anomaly averaged within five days. Likewise, the \overline{SSHA} and \overline{SSTA} are SSH anomaly and the sea surface temperature anomaly (SSTA) averaged over the same days, respectively. The $\overline{T100A}$ is the potential temperature anomaly at 100 m below the water. \overline{UgResA} and \overline{VgResA} are vertical shear of zonal current speed anomaly and vertical shear of meridional current speed anomaly, respectively.

For the first time, Hart et al. [30] used the composite analysis to examine the SST response averaged based on a TC-centered $5^\circ \times 5^\circ$ box during the TC passage. The signal-to-noise ratio is improved by the composite analysis, which reduces the fluctuation related to the mesoscale and submesoscale [21], [31]. This study uses composite analysis to derive the average characteristics for each variable response in the upper ocean. For each upper-ocean variable, the climatological seasonal cycles were subtracted on each grid to obtain an anomaly.

Regarding the response variables, the daily SSHA values from the 1st to the 30th days after the TC passage were considered. The climatological seasonal cycles on each grid were subtracted to produce the temporal evolution of the 30-day SSHAA values. The area-mean value of each oceanic variable was also averaged over the TC-centered $5^\circ \times 5^\circ$ box following the same approach described by [30]. If land exists in the TC-centered box, the invalid values were removed before determining the area-mean value of oceanic variables.

D. Proposed Method

RF is one of the best-known ensemble learning algorithms that combines a set of decision trees (DTs) to construct a stronger predictor by exploiting the idea of bootstrap aggregation [32]. By training multiple DTs with randomly sampled subsets of training data with repetition, RF can effectively reduce the noise within the training data and achieve greater generalization ability. RF is popular due to its good performance and less hyperparameter tuning. Moreover, the RF method has been successfully used in oceanic and atmospheric fields [22], [33]. Thus, the RF was chosen to predict the TC-induced SSHAA, and TC characteristics and prestorm oceanic conditions were used as the input features (i.e., V_{max} , V_{trans} , $R30$, \overline{MLDA} , \overline{SSHA} , \overline{SSTA} , $\overline{T100A}$, \overline{UgResA} , and \overline{VgResA}). The diagram of the data processing flow is given in Fig. 2.

The collected data (17773 points in total) were divided into two groups, with two-third of them for training and the remaining one-third for testing. The data that were used for training the model by dividing into two subgroups: 60% for training and 40% for validation. To avoid overfitting, a grid search method of five-fold cross-validation was employed in order to determine the major parameters of the RF model. The test set provides an unbiased evaluation of the model's performance because it is not used during the training stage. Then the RF model was implemented to simulate the temporal evolution of SSHAA influenced by TCs.

E. Model Evaluations

To evaluate the effectiveness of the RF method, we compared it with the following three mainstream approaches, namely, linear regression (LR) [34], multilayer perceptron (MLP) [35],

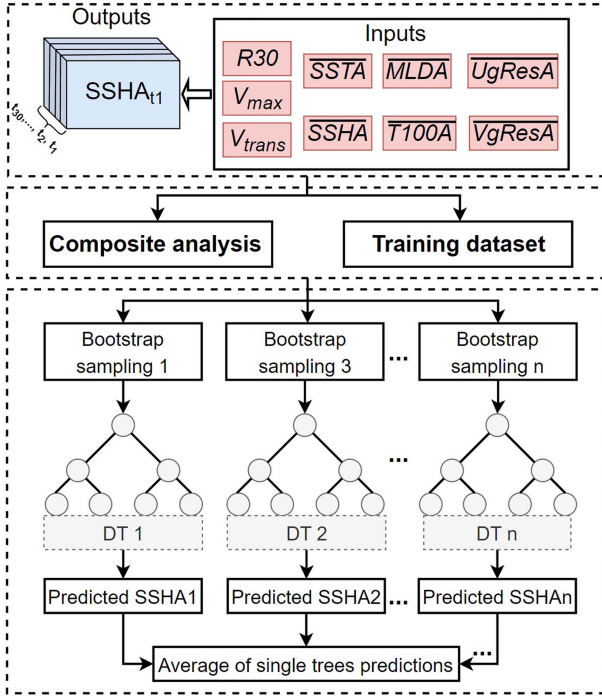


Fig. 2. Schematic diagram of data processing workflow. The subscript, i.e., t_1, t_2, \dots, t_{30} , represent the 1st, 2nd, 3rd, ..., 30th days after TC passage, respectively. $\text{SSHA}_{t_1}, \text{SSHA}_{t_2}, \text{SSHA}_{t_3}, \dots, \text{SSHA}_{t_{30}}$ represent the TC-induced SSHA from the 1st, 2nd, 3rd, ..., 30th days after TC passage, respectively.

and eXtreme Gradient Boosting (XGBoost) [36]. The performance of these machine learning methods was evaluated using the mean absolute error (MAE), the root of mean squared error (RMSE), and the coefficient of determination (R^2) on the independent test set. The error formulation and performance metric were calculated as follows:

$$R^2 = 1 - \frac{\sum_{i=1}^N (O_i - P_i)^2}{\sum_{i=1}^N (O_i - \bar{O})^2} \quad (1)$$

$$RMSE = \sqrt{\frac{1}{N} \sum_{i=1}^N (O_i - P_i)^2} \quad (2)$$

$$MAE = \frac{1}{N} \sum_{i=1}^N |O_i - P_i| \quad (3)$$

where O_i is the value of an observed sample, P_i is the value of a predicted sample, \bar{O} is the mean by calculating the sum of observations by dividing the number of samples, \bar{P} is the mean by calculating the sum of predictions by dividing the number of samples, N is the total number of samples, and $i = 1, 2, \dots, N$.

Here, the smaller the MAE and RMSE the better performance predicted, while R^2 is the opposite.

III. RESULTS

A. Model Performance on Prediction of TC-Induced SSHA

Fig. 3 displays the scatterplots of observed and predicted SSHA for different days using the RF method, and Table III summarizes the metrics for the daily prediction of different machine

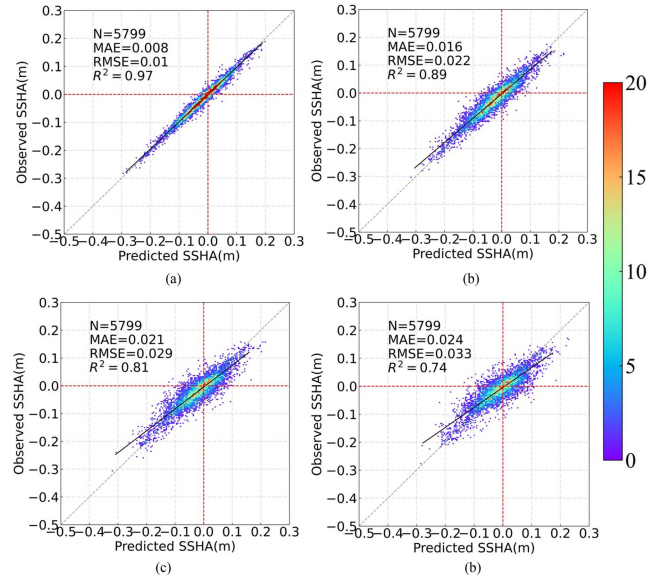


Fig. 3. Scatterplots of observed and predicted TC-induced SSHA for different days using the RF method. (a), (b), (c), and (d) are the 1st, 9th, 17th, and 25th days after the TC passage, respectively. The color represents the density of the number of samples.

TABLE III
DAILY PREDICTION RESULTS (MAE, RMSE, AND R^2) USING DIFFERENT MACHINE LEARNING METHODS

Method	Metrics	Daily			
		1	9	17	25
LR	MAE(m)	0.009	0.020	0.027	0.032
	RMSE(m)	0.012	0.026	0.034	0.040
	R^2	0.970	0.850	0.730	0.610
	MAE(m)	0.008	0.019	0.026	0.030
MLP	RMSE(m)	0.011	0.025	0.033	0.038
	R^2	0.970	0.860	0.750	0.650
	MAE(m)	0.008	0.017	0.023	0.026
	RMSE(m)	0.010	0.022	0.003	0.034
XGBoost	R^2	0.980	0.890	0.790	0.720
	MAE(m)	0.008	0.016	0.021	0.024
	RMSE(m)	0.010	0.022	0.029	0.033
	R^2	0.970	0.890	0.810	0.740

The bold entities indicate the best metrics.

learning methods. The results show that MLP, XGBoost, and RF offer comparable performances in predicting the SSHA of the 1st day after TC passage. On the 9th day after TC passage, the results of XGBoost and RF become very close and are better than LR and MLP. Starting from the 17th day, the predicted SSHA by RF becomes more accurate than LR, MLP, and XGBoost. Its R^2 , i.e., 0.81 and 0.74 for poststorm the 17th and 25th days are greater than that of LR, MLP, and XGBoost. Table III also shows that the long-term prediction stability of the RF method is better than that of the LR, MLP, and XGBoost. Thus, the RF is better suited to capturing this nonlinear relationship between TC-induced SSHA and predictors.

To evaluate the RF model's performance on SSHA induced by TCs of different categories, we quantified these metrics (i.e., MAE, RMSE, and R^2) of predicted SSHA for TCs of different intensities (see Fig. 4). In this study, the categories of TCs are

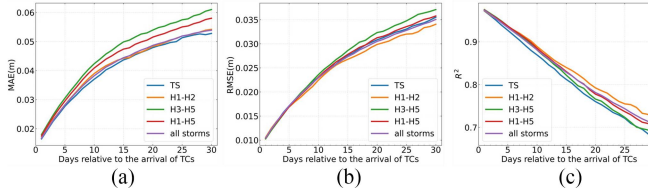


Fig. 4. Assessment of predicted composite area-mean SSHAA considering TCs of different categories: TS (blue), H1-H2 (yellow), H3-H5 (green), H1-H5 (red), and all storms (purple). (a), (b), and (c) represent the MAE, RMSE, and R^2 for a TC-centered $5^\circ \times 5^\circ$ box, respectively. Abbreviations: TS, tropical storm; H1-H2, category 1-2 hurricane; H3-H5, category 3-5 hurricane; and H1-H5, category 1-5 hurricane; all storms, all tropical storms and hurricanes.

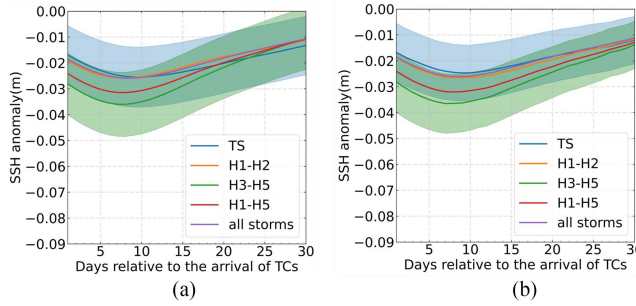


Fig. 5. (a) Temporal evolution of composite area-mean SSHAA for a TC-centered $5^\circ \times 5^\circ$ box in association with passage of TCs based on the observations used in the testing stage. Error width are calculated as the standard deviation divided by the square root of the number of observations of the test set (i.e., standard error of the mean) and are shown by the width of the blue shading and green shading for TS and H3-H5 TCs, respectively. (b) As in (a), but from the predictions.

classified by the Saffir–Simpson scale, i.e., TS: tropical storm ($17.5 \text{ m/s} < \text{the maximum sustained wind speed } V_{max} < 33 \text{ m/s}$), H1: category-1 hurricane, ..., H5: category-5 hurricane, H1-H2: category-1–2 hurricane ($33 \text{ m/s} \leq V_{max} < 50 \text{ m/s}$), H3-H5: category-3–5 hurricane ($V_{max} \geq 50 \text{ m/s}$), H1-H5: category-1–5 hurricane. It should be noted that the term “all storms” refers to all tropical storms and hurricanes.

It can be seen from Fig. 4 that the RF method always performs better in predicting the near-future TC-induced SSHAA values than the far-future values, regardless of the categories of TCs. Within ten days after the TC passage, for TCs of different intensities, the accuracy of the predictions made by RF is comparable. However, between 10 and 30 days, the accuracy of predictions made by the RF on TCs of various intensities begins to diverge. Based on the MAE and RMSE, the prediction accuracy tends to decrease as the TC intensity increases. For TCs of H3-H5, the MAE and RMSE are the highest. This may be because as the TC intensity increases, the amplitude of TC-induced SSHAA is more prominent. The temporal evolution of composite area-mean SSHAA for observations and predictions is consistent with previous research (Fig. 5) [8].

B. Sensitivity Analysis for Various TC-Centered Box Sizes

In composite analysis, TC-centered box size may affect the value of area-mean SSHAA. To examine the sensitivity of the

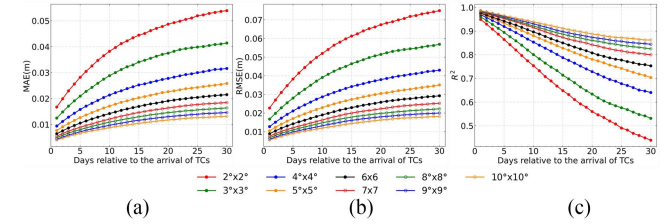


Fig. 6. Evaluation for the test set based on different TC-centered box sizes. (a), (b), and (c) represent MAE, RMSE, and R^2 , respectively. The solid lines with circles of different colors represent different TC-centered box sizes, i.e., $2^\circ \times 2^\circ$, $3^\circ \times 3^\circ$, $4^\circ \times 4^\circ$, $5^\circ \times 5^\circ$, $6^\circ \times 6^\circ$, $7^\circ \times 7^\circ$, $8^\circ \times 8^\circ$, $9^\circ \times 9^\circ$, and $10^\circ \times 10^\circ$.

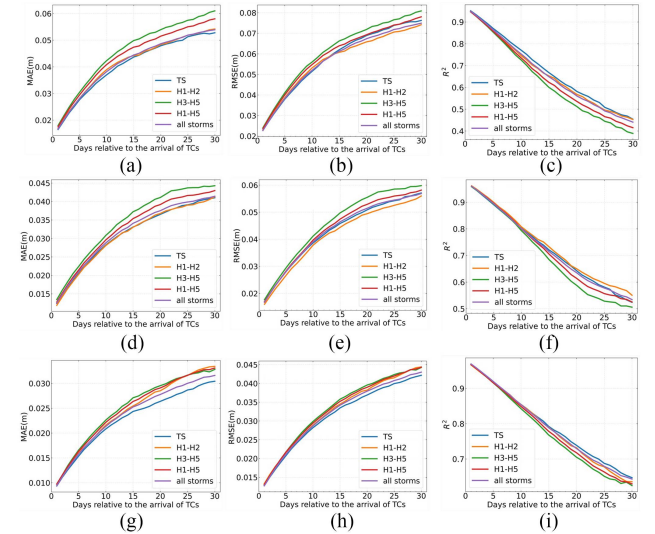


Fig. 7. (a), (d), (g) As in Fig. 4(a), and (b), (e), (h) as in Fig. 4(b), and (c), (f), (i) as in Fig. 4(c), but for different TC-centered box sizes, i.e., $2^\circ \times 2^\circ$, $3^\circ \times 3^\circ$, $4^\circ \times 4^\circ$.

RF method with respect to the various box sizes, we replaced the TC-centered $5^\circ \times 5^\circ$ box to other sizes, including $2^\circ \times 2^\circ$, $3^\circ \times 3^\circ$, $4^\circ \times 4^\circ$, $6^\circ \times 6^\circ$, ..., $10^\circ \times 10^\circ$, and reran the RF model. Then, RF model performance was evaluated with these TC-centered boxes. Independent of the metrics used, the model performance varies in similar patterns as a function of time relative to TC passage for all box sizes [see Fig. 6(a)–(c)]. Another interesting finding from Fig. 6 is that for a fixed TC-centered box size, the MAE and RMSE of the far-future SSHAA predictions are always greater than the near-future predictions, while R^2 is always lower. This is because the correlation between the near-future SSHAA and input features is higher than that of the far-future SSHAA.

Likewise, the temporal evolutions of these metrics are very similar, independent of the TC-centered box size and TC intensity (see Fig. 7). As expected, TC-induced SSHAA amplitude by intensive TCs is more significant for a fixed box size, and the corresponding predicted accuracies are less. Moreover, the amplitudes of SSHAA generated by TCs of category-3–5 hurricane intensity are the strongest, and that of SSHAA produced by TCs of tropical storm intensity is the weakest (see Fig. 8). This amplitude of TC-induced SSHAA is more evident for a TC-centered

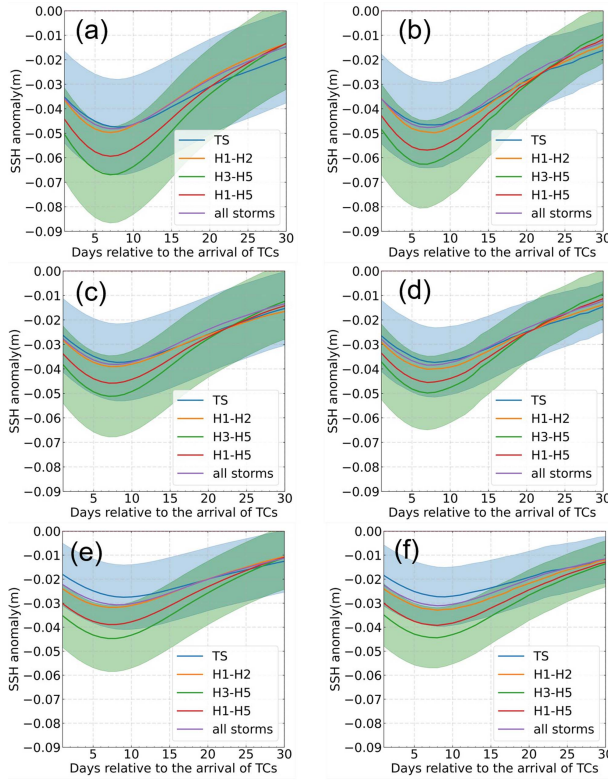


Fig. 8. (a), (c), (e) As in Fig. 5(a), and (b), (d), (f) as in Fig. 5(b), but for different TC-centered box sizes, i.e., $2^\circ \times 2^\circ$, $3^\circ \times 3^\circ$, $4^\circ \times 4^\circ$, respectively.

box size smaller than $5^\circ \times 5^\circ$. This is due to the fact that the increase in the box size will lower the amplitude of TC-induced SSHA as a larger TC-centered box covers greater regions that may not be affected by the TC, leading to the area-mean value being weaker. Despite the fact that the RF method fits better on the relatively weak amplitude of TC-induced SSHA, a $5^\circ \times 5^\circ$ box size may be a suitable tradeoff to balance the model performance and the amplitude of TC-induced SSHA.

C. Evaluation for Spatial Distribution of TC-Induced SSHA

To evaluate the spatial distribution of predictions, the same metrics were quantified. To make the comparison of predictions and observations clearer, resampling was implemented per 20 TC-centered points averaged along the latitudinal direction from south to north. The p -values were calculated to show the significance level between predictions and observations by using a Student's t -test.

As one can see from Fig. 9, the performance of the proposed method on the SSHA of the 1st day after TC passage in terms of MEA, RMSE, and R^2 are 0.002 m, 0.003 m, and 0.98, respectively; the prediction performance on the SSHA of the 9th day after TC passage are $MAE = 0.004$ m, $RMSE = 0.005$ m, and $R^2 = 0.95$; the prediction performance on the SSHA of the 17th day are $MAE = 0.005$ m, $RMSE = 0.006$ m, and $R^2 = 0.92$; the prediction performance on the SSHA of the 25th day after TC passage are $MAE = 0.005$ m, $RMSE = 0.006$ m, and $R^2 = 0.89$. The statistical analysis results show that for all four time periods, the calculated p -values are less than 0.001. This

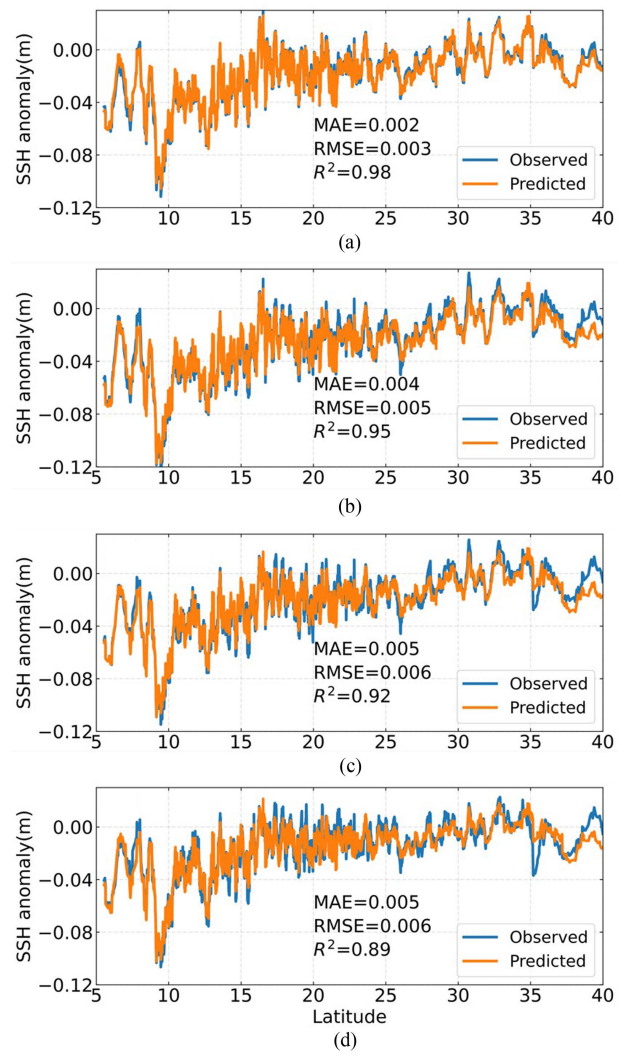


Fig. 9. Estimation of TC-induced SSHA for a TC-centered $5^\circ \times 5^\circ$ box along the latitudinal direction. Yellow solid lines denote observed TC-induced SSHA, while the blue solid lines denote predicted TC-induced SSHA. (a), (b), (c), and (d) are the 1st, 9th, 17th, and 25th days after the TC passage, respectively.

suggests a significant correlation exists between the predicted values made by the RF method and observed values in the spatial distribution.

The averaged amplitudes of observed SSHA in the study area on the 1st, 9th, 17th, and 25th days after tropical cyclones are—0.0194 m, -0.0269 m, -0.0221 m, and -0.0161 m, respectively. For a specific day after TC passage, the RMSE is much lower than the observed mean value of SSHA influenced by tropical cyclones. In addition, the results show that the amplitude of the TC-induced SSHA becomes weaker as time progresses. Regarding the recovery of SSHA after the TC passage, both observations and predictions show a consistent recovery trend (see Fig. 9).

D. Model Performance for the SCS and the WNPSO

The performance of the proposed method is further evaluated based on the data collected in the SCS and WNPSO areas.

TABLE IV
DAILY PREDICTION RESULTS (MAE, RMSE, AND R^2) FOR DIFFERENT REGIONS

Regions	Metrics	Daily			
		1	9	17	25
SCS	MAE(m)	0.007	0.014	0.017	0.017
	RMSE(m)	0.010	0.020	0.024	0.022
	R^2	0.950	0.810	0.730	0.750
WNPSO	MAE(m)	0.008	0.017	0.023	0.027
	RMSE(m)	0.010	0.023	0.031	0.036
	R^2	0.970	0.880	0.770	0.680

The bold entities indicate the best metrics.

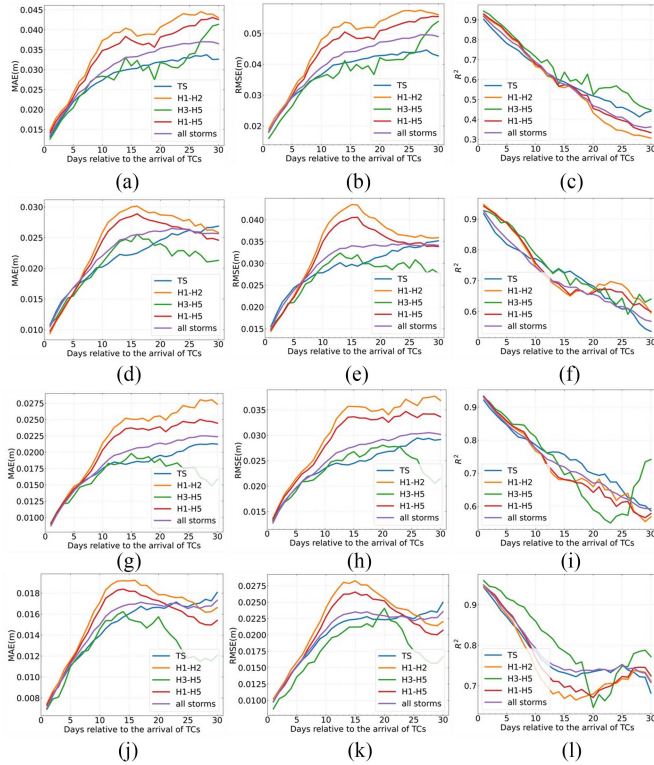


Fig. 10. (a), (d), (g), (j) As in Fig. 4(a), and (b), (e), (h), (k) as in Fig. 4(b), and (c), (f), (i), (l) as in Fig. 4(c), respectively, but for the SCS.

In this example, the performance was measured in terms of MAE, RMSE, and R^2 calculated based on the prediction results on the 1st, 9th, 17th, and 25th days' SSHA after TC passage (see Table IV), with the TC-centered $5^\circ \times 5^\circ$ box.

For the 1st, 9th, and 17th days after the TC passage, R^2 for the WNPSO is 0.97, 0.88, and 0.77, respectively, better than for the SCS is 0.95, 0.81, and 0.73. The MAE and RMSE in the SCS are better than in the WNPSO. The MAE in the SCS achieves 0.007 m, 0.014 m, 0.017 m, and 0.017 m for the 1st, 9th, 17th, and 25th days, respectively, and are better than in the WNPSO. As expected, both RMSE and MAE gradually increase, and R^2 decreases in the WNPSO. Interestingly, it is observed in the SCS that MAE and RMSE begin to level off after the 9th day, as confirmed in Fig. 10.

With different TC-centered boxes (i.e., $2^\circ \times 2^\circ$, $3^\circ \times 3^\circ$, $4^\circ \times 4^\circ$, and $5^\circ \times 5^\circ$), we also calculated the metrics to quantify the performance of the RF method in predicting the temporal evolution of SSHA produced by TCs of different intensity over

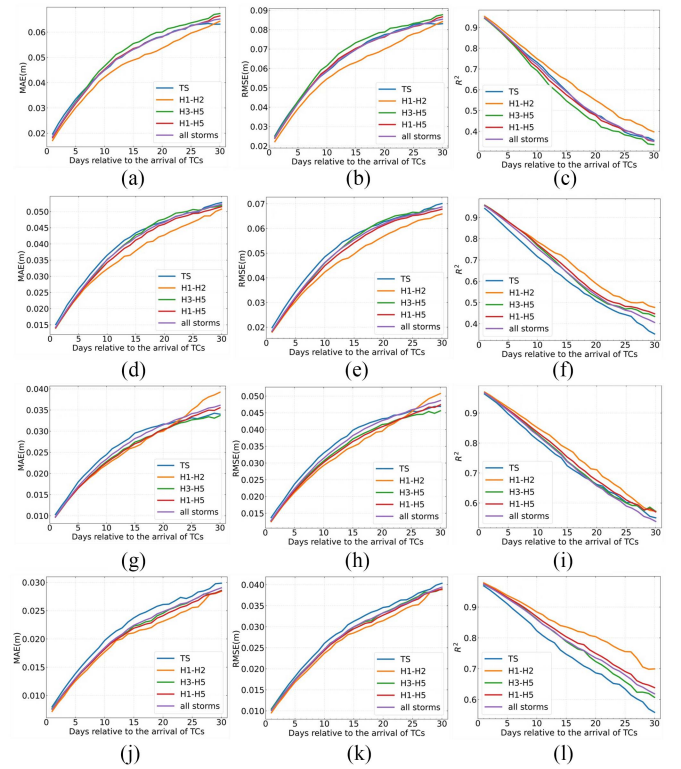


Fig. 11. (a), (d), (g), (j) As in Fig. 4(a), and (b), (e), (h), (k) as in Fig. 4(b), and (c), (f), (i), (l) as in Fig. 4(c), respectively, but for the WNPSO.

these two regions. For the SCS, the evolutions of MAE and RMSE have a similar pattern, independent of the TC-centered box size (see Fig. 10). Both the RMSE and MAE increase rapidly from the 1st day to the 14th days after TC passage, followed by both leveling off. The predictions for TCs of category H1-H2 have the highest RMSE and MAE, followed by TCs of category H1-H5. The RF's performance shows a modest dependence on TC intensity in terms of R^2 .

In the WNPSO, the evolutions of these metrics exhibit a consistent pattern, independent of the box size (see Fig. 11), and are similar to that shown in Figs. 4 and 7. For a fixed box size, predictions for TCs of category H1-H2 achieve the lowest MAE, RMSE, and the lowest R^2 . Moreover, the metrics were also improved by increasing the box size and are consistent with that shown in Fig. 10. Furthermore, the highest RMSE and MAE for the predictions in the SCS were observed to be from TCs of category-1-2 hurricane, while the lowest of those in the WNPSO were found.

IV. DISCUSSIONS

Experimental results presented in this section have shown that the proposed method could precisely predict the amplitude of TC-induced SSHA, with satisfactory robustness in both temporal and spatial domains. In addition, a sensitivity analysis showed that the performance of the RF method presents better in a TC-centered larger box size. Furthermore, the proposed method was evaluated in two different regions, i.e., the SCS

and the WNPSO, and showed strong stability over both regions, though slight variability in predictions of TC-induced SSHA was observed for TCs of varying intensity groups. Finally, a comparison between the numerical model and the RF method showed that predictions are comparable and that the latter even outperforms the former in the short-term predictions.

To understand the differences between machine learning-based predictions and physical model-based simulations [37], [38], [39], a comparison between a typically numerical product and observed SSHA after the TC passage was performed. The numerical data for sea surface height were produced from the daily Global Reanalysis Multi-Ensemble Product GRE, with a spatial resolution of $0.25^\circ \times 0.25^\circ$, which is available from the CMEMS. With the TC-centered $5^\circ \times 5^\circ$ box, the procedures for generating the testing set of numerical data are the same as producing the testing set of observed data. The Student's *t*-test also was also used to calculate the *p*-value in assessing whether the differences between the observed values and numerical values are statistically significant.

The results show that for the 1st day, the MAE = 0.009 m, RMSE = 0.011 m, and R^2 = 0.66; for the 9th, 17th, and 25th days after TC passage, the MAE = 0.005 m, RMSE = 0.006 m, and R^2 = 0.91 (see Fig. 12). The statistical analysis shows that the *p*-values are less than 0.001 for all four periods. This indicates that numerical values are significantly correlated with the observed values in the spatial distribution of the TC-induced SSHA. For the 1st, 9th, and 17th days, the predictions of the RF method outperform that of the numerical model. The predicted SSHA for the RF method still is comparable to that for the numerical models on the 25th day (see Fig. 9).

The performance of the numerical model is time-independent, except for the 1st day. The RF methods' performance is time-dependent because the prestorm oceanic averaged variables are used as input features. Previous studies have also demonstrated that ML-based methods exhibit superior performance in short-term predictions when compared to long-term predictions [40], [41]. It can be observed that both types of approaches have their own advantages in predicting the temporal evolution of TC-induced SSHA in terms of the time scales.

The metrics (i.e., MAE, RMSE, and R^2) evaluated on the predicted TC-induced SSHA have shown that uncertainties are more evident for strong TCs than for weak TCs. Furthermore, residuals quantified between the observed and predicted values show that observed SSHA is stronger than predicted SSHA for TCs of TS intensity, while the SSHA generated by TCs of H1-H5 intensity is stronger in the predictions than the observations (see Fig. 13). This suggests that the RF method underpredicted the SSHA for TCs of tropical storm intensity and overpredicted it for TCs of hurricane intensity, due to changes in the signal-to-noise ratio [21].

This study found that the prediction uncertainties vary with which region the model is applied. For example, TCs of category-1-2 hurricane for the predictions of TC-induced SSHA has the highest RMSE and MAE in the SCS, which have the lowest RMSE and MAE in the WNPSO. On the other hand, the evolutions of these metrics are inconsistent in these two regions, whereas they coincide well in the WNPSO and the

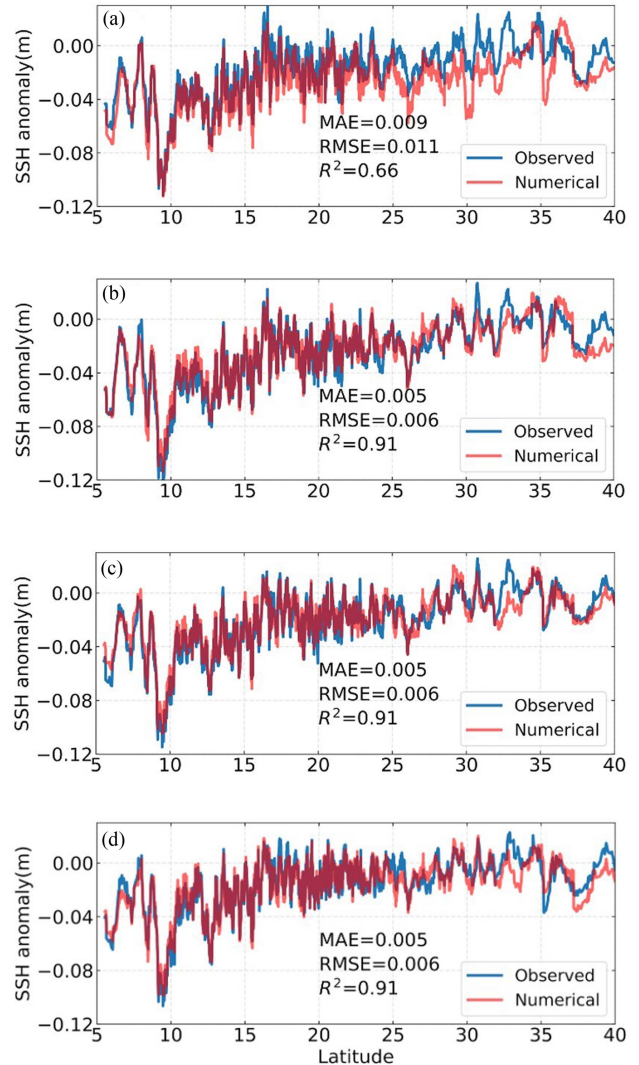


Fig. 12. (a), (b), (c), and (d) As in Figs. 9(a), 9(b), 9(c), and 9(d), respectively, but the red solid lines denote the numerical model.

whole study area. As the SCS is a marginal sea, the passage of TCs is influenced by the topography of the area, which in turn may change some TC characteristics (e.g., intensity and translation speed). At the same time, changes in TC-induced SSHA can be significant in nearshore regions. However, in open sea (e.g., WNPSO), TC movement is not controlled by such topography [12], [42], [43], [44]. These uncertainties in ML-based predictions may therefore be potentially influenced by the geographical location, in addition to being controlled by TC characteristics and preexisting ocean factors.

Further improvements are still needed for the proposed method. First, adding more training data of the extreme SSHA values induced by some TC cases for model training might further improve the model performance. Previous studies have reported that such TC (Typhoon Damrey, 2005) can even trigger an intensive amplitude of SSHA up to -0.25 m along the TC track for the 1st day after the TC passage [12]. The low occurrence of such TC cases per year, with only a few samples, leads to reduced generalization ability of the ML methods. Second,

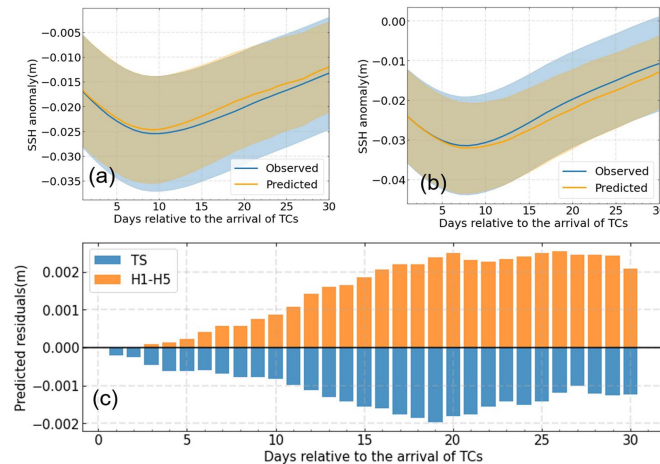


Fig. 13. (a) Temporal evolution of composite area-mean SSHA for a TC-centered $5^\circ \times 5^\circ$ box in association with passage of TCs for TS intensity based on predictions and observations used in the testing stage. Error width is calculated as in Fig. 5(a) and are shown by the width of the blue shading and yellow shading for observations and predictions, respectively. (b) As in (a), but for the TCs of H1-H5 intensity. (c) Predicted residuals are calculated by subtracting the predicted values from observed values. The yellow and blue represent the predicted residuals for TS and H1-H5 intensities, respectively.

the reason for the underpredicted SSHA for weak TCs and the overpredicted SSHA for strong TCs would be further explored. Moreover, coupling the ML methods and numerical models to improve TC-induced SSHA predictions would be a promising attempt.

V. CONCLUSION

In this study, a composite analysis-based RF method is proposed to infer the daily TC-induced SSH field, and it is evaluated in the WNP where TCs are the most active. In this proposed method, a composite analysis is employed to capture the amplitude of the TC wind pump induced SSH. The proposed method considers atmospheric and oceanic parameters as input features to weigh the contributions of both TC characteristics and pre-storm ocean conditions to the TC-induced SSH. The results of the experiment demonstrate the effectiveness of the proposed method in accurately predicting the amplitude of the TC-induced SSH. The method displays satisfactory robustness in both the temporal and spatial domains. Moreover, the RF method was found to be better to a larger TC-centered box. Furthermore, the proposed method was examined in two distinct regions and displayed strong stability across both regions. Eventually, a comparison between the numerical model and the machine learning method revealed that the latter outperformed the former in short-term predictions, with the two methods producing comparable results in general. In short, the study provides insight on the application of machine learning to improve the prediction of SSH influenced by extreme weather conditions.

ACKNOWLEDGMENT

The author would like to thank Remote Sensing Systems for providing Microwave Imager SST data (www.remss.com);

Copernicus Marine and Environmental Monitoring Service Center for daily altimeter satellite gridded SLA data and the daily Global Reanalysis Multi-Ensemble Product GREP data (<https://resources.marine.copernicus.eu/>); and National Centers for Environmental Information for TC best track data (<https://www.ncdc.noaa.gov/ibtracs/>).

REFERENCES

- [1] S. Brand, "The effects on a tropical cyclone of cooler surface waters due to upwelling and mixing produced by a prior tropical cyclone," *J. Appl. Meteorol.*, vol. 10, no. 5, pp. 865–874, 1971.
- [2] K. A. Emanuel, "The dependence of hurricane intensity on climate," *Nature*, vol. 326, no. 6112, pp. 483–485, 1987.
- [3] J. E. Geisler, "Linear theory of the response of a two layer ocean to a moving hurricane," *Geophysical Astrophysical Fluid Dyn.*, vol. 1, no. 1-2, pp. 249–272, 1970.
- [4] L. K. Shay, S. W. Chang, and R. L. Elsberry, "Free surface effects on the near-inertial ocean current response to a hurricane," *J. Phys. Oceanogr.*, vol. 20, no. 9, pp. 1405–1424, 1990.
- [5] L. K. Shay and S. W. Chang, "Free surface effects on the near-inertial ocean current response to a hurricane: A revisit," *J. Phys. Oceanogr.*, vol. 27, no. 1, pp. 23–39, 1997.
- [6] J. Zhou, P. Li, and H. Yu, "Characteristics and mechanisms of sea surface height in the South China Sea," *Glob. Planet. Change*, vol. 88, pp. 20–31, 2012.
- [7] K. Kang and I. Moon, "Sea surface height changes due to the tropical cyclone-induced water mixing in the Yellow Sea, Korea. Front," *Earth Sci.*, vol. 10, 2022, Art. no. 826582.
- [8] W. Mei, F. Primeau, J. C. McWilliams, and C. Pasquero, "Sea surface height evidence for long-term warming effects of tropical cyclones on the ocean," *Proc. Nat. Acad. Sci. USA*, vol. 110, no. 38, pp. 15207–15210, 2013, doi: [10.1073/pnas.1306753110](https://doi.org/10.1073/pnas.1306753110).
- [9] D. B. Chelton and M. G. Schlax, "Global observations of oceanic Rossby waves," *Science*, vol. 272, no. 5259, pp. 234–238, 1996.
- [10] P. S. Polito and P. Cornillon, "Long baroclinic Rossby waves detected by TOPEX/POSEIDON," *J. Geophysical Res., Oceans*, vol. 102, no. C2, pp. 3215–3235, 1997, doi: [10.1029/96JC03349](https://doi.org/10.1029/96JC03349).
- [11] Y.-C. Zhang, L.-F. Zhang, and Q.-P. Lü, "Dynamic mechanism of interannual sea surface height variability in the North Pacific Subtropical Gyre," *Adv. Atmospheric Sci.*, vol. 28, no. 1, pp. 158–168, Jan. 2011, doi: [10.1007/s00376-010-0038-8](https://doi.org/10.1007/s00376-010-0038-8).
- [12] G. M. Zheng and D. Tang, "Offshore and nearshore chlorophyll increases induced by typhoon winds and subsequent terrestrial rainwater runoff," *Mar. Ecol. Prog. Ser.*, vol. 333, pp. 61–74, 2007.
- [13] G. Pan, D. Tang, and Y. Zhang, "Satellite monitoring of phytoplankton in the East Mediterranean Sea after the 2006 Lebanon oil spill," *Int. J. Remote Sens.*, vol. 33, no. 23, pp. 7482–7490, 2012.
- [14] R. L. Srivastava, N. M. Urban, R. Olson, and K. Keller, "Toward a physically plausible upper bound of sea-level rise projections," *Climatic Change*, vol. 115, no. 3, pp. 893–902, 2012.
- [15] J. Chen, C. Wilson, D. Chambers, R. Nereim, and B. Tapley, "Seasonal global water mass budget and mean sea level variations," *Geophysical Res. Lett.*, vol. 25, no. 19, pp. 3555–3558, 1998.
- [16] T. Niedzielski and W. Kosek, "Forecasting sea level anomalies from TOPEX/Poseidon and Jason-1 satellite altimetry," *J. Geodesy*, vol. 83, no. 5, pp. 469–476, 2009.
- [17] S. Barbosa, M. Silva, and M. Fernandes, "Multivariate autoregressive modelling of sea level time series from TOPEX/Poseidon satellite altimetry," *Nonlinear Processes Geophys.*, vol. 13, no. 2, pp. 177–184, 2006.
- [18] J. Horstmann, C. Wackerman, S. Falchetti, and S. Maresca, "Tropical cyclone winds retrieved from synthetic aperture radar," *Oceanography*, vol. 26, no. 2, pp. 46–57, 2013.
- [19] Y.-X. Wang, M. Wei, Z.-H. Wang, S. Zhang, and L.-X. Liu, "Novel scanning strategy for future spaceborne Doppler weather radar with application to tropical cyclones," *IEEE J. Sel. Topics Appl. Earth Observ. Remote Sens.*, vol. 10, no. 6, pp. 2685–2693, Jun. 2017.
- [20] Y. Wang, M. Wei, and Q. Shi, "First spaceborne version of velocity-azimuth display technique for wind field retrieval on cloud and precipitation radar," *Atmosphere*, vol. 11, no. 10, 2020, Art. no. 1089.
- [21] W. Mei and C. Pasquero, "Spatial and temporal characterization of sea surface temperature response to tropical cyclones," *J. Climate*, vol. 26, no. 11, pp. 3745–3765, 2013.

- [22] G. E. Jergensen, A. McGovern, R. Lagerquist, and T. Smith, "Classifying convective storms using machine learning," *Weather Forecasting*, vol. 35, no. 2, pp. 537–559, Apr. 2020, doi: [10.1175/waf-d-19-0170.1](https://doi.org/10.1175/waf-d-19-0170.1).
- [23] Z. Xu, H. Zhang, Y. Wang, X. Wang, S. Xue, and W. Liu, "Dynamic detection of offshore wind turbines by spatial machine learning from spaceborne synthetic aperture radar imagery," *J. King Saud Univ. - Comput. Inf. Sci.*, vol. 34, no. 5, pp. 1674–1686, May 2022, doi: [10.1016/j.jksuci.2022.02.027](https://doi.org/10.1016/j.jksuci.2022.02.027).
- [24] I. I. Lin, "Typhoon-induced phytoplankton blooms and primary productivity increase in the western North Pacific subtropical ocean," *J. Geophysical Res., Oceans*, vol. 117, no. 3, 2012, Art. no. C0303, doi: [10.1029/2011JC007626](https://doi.org/10.1029/2011JC007626).
- [25] Y. Sui, J. Sheng, D. Tang, and J. Xing, "Study of storm-induced changes in circulation and temperature over the northern South China Sea during Typhoon Linfa," *Continental Shelf Res.*, vol. 249, Oct. 2022, Art. no. 104866, doi: [10.1016/j.csr.2022.104866](https://doi.org/10.1016/j.csr.2022.104866).
- [26] F. J. Wentz, C. Gentemann, D. Smith, and D. Chelton, "Satellite measurements of sea surface temperature through clouds," *Science*, vol. 288, no. 5467, pp. 847–850, 2000.
- [27] G. Chen, X. Chen, and C. Cao, "Divergence and dispersion of global eddy propagation from satellite altimetry," *J. Phys. Oceanogr.*, vol. 52, no. 4, pp. 705–722, 2022.
- [28] K. R. Knapp, H. J. Diamond, J. P. Kossin, M. C. Kruk, and C. J. Schreck, "2018: International Best Track Archive for Climate Stewardship (IBTrACS) Project, version 4. [indicate subset used]," *NOAA Nat. Centers Environ. Inf.*, doi: [10.25921/82ty-9e16](https://doi.org/10.25921/82ty-9e16).
- [29] T. Nakazawa and S. Hoshino, "Intercomparison of Dvorak parameters in the tropical cyclone datasets over the western North Pacific," *Sola*, vol. 5, pp. 33–36, 2009.
- [30] R. E. Hart, R. N. Maue, and M. C. Watson, "Estimating local memory of tropical cyclones through MPI anomaly evolution," *Monthly Weather Rev.*, vol. 135, no. 12, pp. 3990–4005, 2007.
- [31] Y. Wang, "Composite of typhoon-induced Sea surface temperature and chlorophyll-a responses in the South China Sea," *J. Geophysical Res., Oceans*, vol. 125, no. 10, 2020, Art. no. e2020JC016243.
- [32] L. Breiman, "Random forests," *Mach. Learn.*, vol. 45, no. 1, pp. 5–32, 2001.
- [33] D. Rolnick et al., "Tackling climate change with machine learning," *ACM Comput. Surv.*, vol. 55, no. 2, pp. 1–96, 2022.
- [34] S. Dominik and P. Terray, "Improvement of ENSO prediction using a linear regression model with a southern Indian Ocean sea surface temperature predictor," *Geophysical Res. Lett.*, vol. 32, no. 18, 2005, Art. no. L18702, doi: [10.1029/2005GL023153](https://doi.org/10.1029/2005GL023153).
- [35] X. Feng, G. Ma, S.-F. Su, C. Huang, M. K. Boswell, and P. Xue, "A multi-layer perceptron approach for accelerated wave forecasting in Lake Michigan," *Ocean Eng.*, vol. 211, 2020, Art. no. 107526.
- [36] T. Chen and C. Guestrin, "Xgboost: A scalable tree boosting system," in *Proc. 22nd ACM SIGKDD Int. Conf. Knowl. Discov. Data Mining*, 2016, pp. 785–794.
- [37] J. Wei, G. Q. Jiang, and X. Liu, "Parameterization of typhoon-induced ocean cooling using temperature equation and machine learning algorithms: An example of typhoon Soulik (2013)," *Ocean Dyn.*, vol. 67, no. 9, pp. 1179–1193, 2017, doi: [10.1007/s10236-017-1082-z](https://doi.org/10.1007/s10236-017-1082-z).
- [38] G. Q. Jiang, J. Xu, and J. Wei, "A deep learning algorithm of neural network for the parameterization of typhoon-ocean feedback in typhoon forecast models," *Geophysical Res. Lett.*, vol. 45, no. 8, pp. 3706–3716, 2018, doi: [10.1002/2018GL077004](https://doi.org/10.1002/2018GL077004).
- [39] Z. Zhao, J. Zhou, and H. Du, "Artificial intelligence powered forecast of oceanic mesoscale phenomena: A typhoon cold wake case occurring in Northwest Pacific Ocean," *Future Gener. Comput. Syst.*, vol. 129, pp. 389–398, 2022.
- [40] Q. Shao et al., "A deep learning model for forecasting Sea surface height anomalies and temperatures in the South China Sea," *J. Geophysical Res., Oceans*, vol. 126, no. 7, 2021, Art. no. e2021JC017515.
- [41] Y. Zhou, C. Lu, K. Chen, and X. Li, "Multilayer fusion recurrent neural network for sea surface height anomaly field prediction," *IEEE Trans. Geosci. Remote Sens.*, vol. 60, pp. 1–11, 2021.
- [42] Y. Li and D. Tang, "Tropical cyclone Wind Pump induced chlorophyll-a enhancement in the South China Sea: A comparison of the open sea and continental shelf," *Front. Mar. Sci.*, vol. 9, pp. 1–13, Dec. 2022, doi: [10.3389/fmars.2022.1039824](https://doi.org/10.3389/fmars.2022.1039824).
- [43] W. Mei, C. C. Lien, I. I. Lin, and S. P. Xie, "Tropical cyclone-induced ocean response: A comparative study of the south China sea and tropical northwest Pacific," *J. Climate*, vol. 28, no. 15, pp. 5952–5968, 2015, doi: [10.1175/JCLI-D-14-00651.1](https://doi.org/10.1175/JCLI-D-14-00651.1).
- [44] X. Chen et al., "Estimation of typhoon-enhanced primary production in the South China Sea: A comparison with the Western North Pacific," *Continental Shelf Res.*, vol. 111, pp. 286–293, 2015, doi: [10.1016/j.csr.2015.10.003](https://doi.org/10.1016/j.csr.2015.10.003).



Hongxing Cui is currently working toward the Ph.D. degree in marine environmental science with a Joint Ph.D. Program of Hong Kong University of Science and Technology, Hong Kong, SAR, China and Southern Marine Science and Engineering Guangdong Laboratory (Guangzhou), Guangzhou, China.

His research interests include tropical cyclones, ocean-atmosphere interaction, machine learning, and remote sensing.



Danling Tang received the Ph.D. degree from the Hong Kong University of Science and Technology, Hong Kong, China, in 1998.

She was a Professor with Fudan University, Fudan, China. She is currently a Professor with the Southern Marine Science and Engineering Guangdong Laboratory (Guangzhou), Guangzhou, China, and the South China Sea Institute of Oceanology, Chinese Academy of Sciences, Beijing, China. She is also the Director of Guangdong Remote Sensing Center for Marine Ecology and Environment, Guangzhou, China. She has also serviced for the following scientific communities: The President of the Pan Ocean Remote Sensing Association, the President of PACON International, Councilor of AGU, etc. Her research interests include satellite remote sensing for marine ecology/environment, natural hazard, and global environmental changes.



Huizeng Liu received the Ph.D. degree in geography from Hong Kong Baptist University, Hong Kong, China, in 2019.

He is currently an Assistant Professor with Shenzhen University, Shenzhen, China. His research interests include Moon and deep space-based Earth observation, remote sensing of environment monitoring, ocean color remote sensing, and machine learning modeling.



Yi Sui is currently working toward the Ph.D. degree with the Physical Oceanography Department, Dalhousie University, Halifax, NS, Canada.

He has authored or coauthored approximately ten SCI papers. His research interests include numerical ocean modeling, laboratory physical experiment, and satellite remote sensing observation. His current focus is on the numerical study of temperature, salinity, currents, dissolved oxygen, and associated variability over the eastern Canadian shelf.



Xiaowei Gu received the doctorate degree in computer science from Lancaster University, Lancaster, U.K., in 2018.

He is currently a Lecturer with the School of Computing, University of Kent, Canterbury, U.K. His research interests include machine learning, data analytics, and signal processing.